Investigating non-susceptibility contributions to GRE phase contrast

Karsten Sommer[1], Ferdinand Schweser[1], Andreas Deistung[1], and Jürgen Rainer Reichenbach[1]
[1]*Medical Physics Group, Dept. of Diagnostic and Interventional Radiology I, Jena University Hospital, Jena, Germany*

INTRODUCTION – Quantitative susceptibility mapping (QSM) is a novel imaging technique that determines tissue magnetic susceptibility from conventional gradient-echo (GRE) phase images. While it has been shown that the main part of phase contrast can be explained by the bulk magnetic susceptibility (BMS) of tissue [1], the requirement for strong regularization during reconstruction indicates that non-BMS contributions are present in the phase images. This is confirmed by recent investigations that suggest that local non-BMS effects, such as chemical exchange between water and macromolecules [2] or a non-spherical Lorentzian cavity [3], contribute to phase contrast between gray and white matter. In this contribution, we present a technique for separating BMS and non-BMS effects in phase data and, as a proof-of-principle, demonstrate it with an initial experiment based on simulated data.

MATERIALS AND METHODS – *Regularization:* The inverse field-to-source problem of QSM can be written in matrix-vector notation as $\min_{\chi}\left\|A\vec{\chi}-\vec{\delta}\right\|_2^2$ (1), where $\vec{\chi}$ is the vector representation of the 3D susceptibility map, A is a matrix that replicates a convolution (non-local) with the spatial unit dipole, and $\vec{\delta}$ is a vector that contains the measured background-corrected phase data [4]. Due to the ill-posed nature of this problem, regularization strategies are indispensable to obtain a meaningful solution. Recently, Schweser et al. [4] showed that regularization of (1) can be achieved by introducing an additional solution vector $\vec{\sigma}$ to the problem: $\min_{\chi}\left\|A\vec{\chi}+\vec{\sigma}-\vec{\delta}\right\|_2^2$ (2). Ideally, $\vec{\sigma}$ will account for all contributions in the phase data that cannot be explained by the non-local term $A\vec{\chi}$, i.e. all non-BMS contributions. The high under-determination of the problem in Eq. (2), however, impeded successful separation of both effects [4]. In this study, we address this under-determination by adding spatial-domain constraints on both the BMS and non-BMS contributions using a special weighted total-variation norm:

$$\min_{\chi,\sigma}\left\|A\vec{\chi}+\vec{\sigma}-\vec{\delta}\right\|_2^2+\lambda\left(\left\|\vec{\chi}\right\|_{W-TV}^{(\chi)}+\kappa\left\|\vec{\sigma}\right\|_{W-TV}^{(\sigma)}\right) \quad (3) \qquad \text{where} \quad \left\|\vec{\beta}\right\|_{W-TV}^{(\beta)}=\left\|\hat{W}_x^{\beta}G_x\vec{\beta}\right\|_1+\left\|\hat{W}_y^{\beta}G_y\vec{\beta}\right\|_1+\left\|\hat{W}_z^{\beta}G_z\vec{\beta}\right\|_1 \quad (4) \qquad (\beta=\chi,\sigma).$$

The first term in (3) expresses data fidelity of the field calculated from $\vec{\chi}$ and the second term puts the constraints on $\vec{\chi}$ and $\vec{\sigma}$; λ and κ are regularization parameters. $\hat{W}_i^{\beta}$ in (4) are diagonal representations of binary masks that define regions which are assumed to be homogeneous in the BMS and non-BMS map, respectively, and G_i are gradient operators in the three spatial directions (i=x,y,z). Note that application of different *a priori* information to BMS and non-BMS contributions ($\hat{W}_i^{\chi}\neq\hat{W}_i^{\sigma}$) is possible in this approach. The L1 norm, $\|\cdot\|_1$, promotes sparsity between the edges in the binary masks and the actual edges in the BMS and non-BMS maps [5]. *Numerical model*: To evaluate the algorithm, a numerical model was created by assigning BMS values in the range of -0.2ppm to 0.4ppm to a 3x3 matrix of tubular regions (Fig. 1a). Similarly, non-BMS-related phase values in the range of -0.45rad to +0.6rad were assigned to the same 3x3 matrix of regions (Fig 1b). In both cases, 7 regions had values different to and 2 had values equal to the surrounding medium. The phase map due to BMS was calculated by fast forward-field computation [6] with B_0 = 3T, TE = 20ms and B_0 perpendicular to the cylindrical axes. Finally, the non-BMS model and a pattern of normally distributed noise (standard deviation: 0.1 rad) were added to this map to simulate non-BMS contributions and measurement noise, respectively (Fig. 1c). The binary masks $\hat{W}_i^{\chi}$ and $\hat{W}_i^{\sigma}$ (Fig. 1d) in Eq. (4) were created by applying a threshold (10^{-5}) to the gradient of a binary representation of all 9 tubes. *Implementation*: The minimization problem (3) was solved using a modified version of the NESTA algorithm [7], which is able to handle the *a priori* information conveyed by the binary masks in (4). The following NESTA parameters were used for the calculation in this study: $\mu=0.1$, relative convergence tolerance of 10^{-15}, 20 outer and 40 inner loop iterations. Through empirical optimization, the following regularization parameters (Eq. 3) were found to yield lowest artifact levels : $\lambda=0.06$, $\kappa=0.2$. The reconstructed BMS and non-BMS maps were used to forward calculate the phase map, the mean values in the tubes were correlated to the model data, and linear least squares fitting was performed. To illustrate the inversion artifacts when non-BMS contributions were neglected during QSM, a BMS map was calculated using thresholded k-space division (TKD) [8].

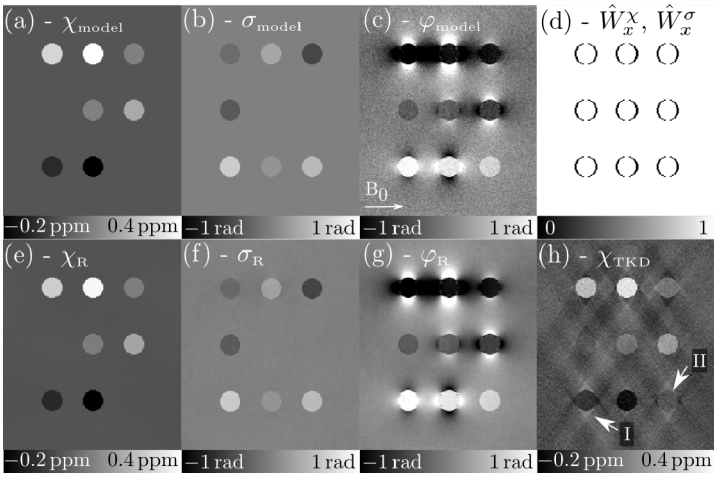

Figure 1. Coronal slices of the BMS model (a), the non-BMS model (b), the phase map calculated using BMS and non-BMS model (c), the binary gradient mask that is used for weighting the gradients in x-direction of both $\vec{\chi}$ and $\vec{\sigma}$, (d), the reconstructed BMS map (e), the reconstructed non-BMS map (f), the reconstructed phase map (g), and the BMS map calculated with the TKD method (h). Arrows I and II indicate artifacts and non-BMS contributions in the TKD map, respectively.

RESULTS – The calculated BMS and non-BMS maps, χ_R and σ_R (Fig. 1e,f), revealed excellent agreement with the model. The difference map $\varphi_R-\varphi_{model}$ (not shown) exhibited predominantly noise. In contrast to this, the susceptibility map calculated with the TKD algorithm was corrupted by streaking artifacts, high noise level and contained non-BMS contributions (arrows in Fig. 1h). Fitting of the mean values in the 9 tubes of the BMS and non-BMS maps to the model data showed only minor underestimation (~ 3%) of susceptibility values (Fig. 2a,b).

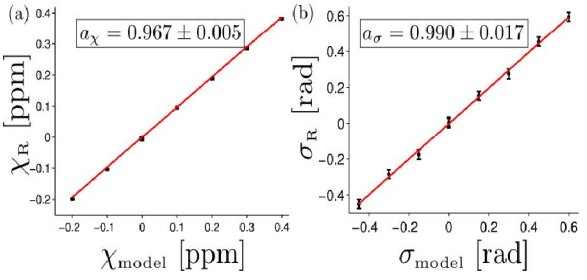

Figure 2. Comparison of the mean values of the reconstructed BMS map in all 9 tubes with the values of the model, and the result of the linear fit (r=0.9992, $p<5\cdot10^{-11}$) (a). The same for the non-BMS map (r=0.9999, $p<8\cdot10^{-14}$) (b).

DISCUSSION AND CONCLUSIONS – In this study, separation of BMS and non-BMS contributions in phase images was performed using high-quality *a priori* information. The presented preliminary results demonstrate feasibility of separating both effects. The algorithm could, thus, enable detailed investigations of non-BMS contributions to the observed cortical GM/WM phase contrast *in vivo*. However, further investigations are needed to examine the technique's applicability to *in vivo* data and its performance with imperfect *a priori* information. *In vivo*, high-quality priors could be obtained using manual segmentation of the cortex in phase images or by taking into account different sources of *a priori* information, such as GRE magnitude, phase, and R_2^* maps.

REFERENCES – [1] Schweser F et al., 2011. *NeuroImage*. 54:2789-807. [2] Shmueli K et al., 2011. *Magn Reson Med*. 65(1):35-43. [3] He X et al., 2009. *PNAS* 106(32):13558-63. [4] Schweser F et al., 2010. *Med Phys*. 37(10):5165-78. [5] Candès E J et al. 2007. *J Four Anal Appl* 14(5):1-28. [6] Holt R W et al. 1994. *J Magn Res Imag*. 4(6):809-18. [7] Becker, S et al., 2011. *SIAM J Imag Sci*. 4(1):1-39. [8] Shmueli K et al., 2009. *Magn Reson Med*. 62(6):1510-22